npj | climate and atmospheric science

Article

Published in partnership with CECCR at King Abdulaziz University

https://doi.org/10.1038/s41612-025-01187-6

Trans-basin interaction sustains multi-year marine heatwaves in the Gulf of Alaska

Yu Zhao[1], Jin-Yi Yu[1] ✉, Huang-Hsiung Hsu[2], I-I Lin[3], Song Yang[4,5], Chunzai Wang[6,7,8], Jian Shi[9,10], Yan Du[11], Xin Wang[6,7], Tao Lian[12] & Sang-Wook Yeh[13]

Multi-year marine heatwaves (MHWs) in the Gulf of Alaska (GOA) are major climate events with lasting ecological and economic effects. Though often seen as local Pacific phenomena, our study shows their persistence depends on trans-basin interactions between the North Pacific and North Atlantic. Using observational data and climate model experiments, we find that prolonged MHWs occur as sequential warming episodes triggered by atmospheric wave trains crossing ocean basins. These wave trains alter surface heat flux, initiating MHWs in the GOA and changing North Atlantic sea surface temperatures (SSTs). In turn, Atlantic SST anomalies reinforce wave activity, fueling subsequent MHW episodes in a feedback loop. This mechanism appears in historical events (1949–52, 1962–65, 2013–16, and 2018–22), highlighting MHWs as a trans-basin phenomenon. Our findings link GOA MHWs to trans-basin atmospheric wave dynamics and identify North Atlantic SSTs as a potential predictor of their duration.

Marine heatwaves (MHWs) in the northeastern Pacific, particularly near the Gulf of Alaska (GOA), have drawn considerable attention due to their remarkable intensity, prolonged duration, and vast spatial extent[1–8]. Events like the "Pacific warm blob"— characterized by anomalously warm waters persisting from 2013 to 2016 and re-emerging in 2018 to continue until at least 2022— highlight the enduring and impactful nature of these phenomena[1,9,10]. These multi-year MHWs have caused substantial ecological and economic disruptions, including marine food web alterations, hazardous algal blooms, and devastating impacts on fisheries along the west coast of North America[11–16].

Current understanding attributes GOA MHWs primarily to persistent anomalous high-pressure systems over the region[9,10,17–19]. These systems can persist for extended periods, driving MHWs through surface heat flux (SHF) anomalies—reducing ocean heat loss during winter and enhancing solar radiation absorption under clearer skies in summer[17,18]. However, the pronounced extratropical seasonal cycle—marked by substantial shifts in atmospheric and oceanic conditions between seasons—can disrupt the persistence of surface ocean temperature anomalies, making it challenging for such variations to be maintained over extended periods[20]. Additionally, the relatively weak local atmosphere-ocean coupling in the mid-latitudes limits the ocean's ability to influence overlying atmospheric patterns[21], making it difficult for oceanic temperature anomalies to reinforce or maintain the atmospheric conditions that initially generated them. Together, these factors tend to dissipate warm anomalies and hinder their persistence beyond a single season or year. This raises a crucial question: What mechanisms allow GOA MHWs to be sustained on multi-year timescales?

Emerging evidence suggests a potential mechanism rooted in trans-basin atmospheric dynamics. Recent studies indicate that the high-pressure anomalies linked to GOA MHWs are part of a larger trans-basin wave train originating in the tropical Pacific and extending into the North Atlantic[7,22,23]. As this wave train propagates across the Pacific-Atlantic sector, it not only triggers MHWs in the GOA but also induces a distinct tripolar pattern of sea surface temperature anomalies (SSTAs) in the North Atlantic—characterized by mid-latitude warming flanked by subpolar and subtropical cooling[7]. Previous studies on trans-basin interactions show that North Atlantic SSTAs can influence the Pacific via atmospheric teleconnections, including modifications to the Walker Circulation and Gill-type responses[24–29]. If such Atlantic feedback can reactivate the trans-basin wave trains, they offer a plausible mechanism for sustaining multi-year MHWs in the GOA.

Building on these insights, we propose a trans-basin interaction mechanism to explain the occurrence of multi-year MHWs in the GOA region. In this framework, the trans-basin wave train initiates both GOA MHW episodes and Atlantic SSTAs, with the latter feeding back to influence Pacific atmospheric conditions and

A full list of affiliations appears at the end of the paper. ✉e-mail: jyyu@uci.edu

reactivate the wave trains. This reactivation triggers subsequent MHW episodes, forming a sequence of interconnected warming events that sustain elevated temperatures over multiple years. Rather than viewing multi-year MHWs as continuous warming, we interpret them as a series of discrete, wave train-induced episodes sustained by a self-reinforcing feedback loop, which persists until disrupted by other climate variability modes or internal atmospheric fluctuations.

To validate this hypothesis, we proceed through several key steps. First, we identify key forcing regions in the Pacific where anomalous ascending motion (upward air movement that promotes convection) initiates trans-basin wave trains. Next, we demonstrate that North Atlantic SSTAs, induced by these wave trains, can in turn trigger ascending motion in the same Pacific regions, thereby reactivating the wave trains. Finally, we show that this self-reinforcing feedback loop—comprising trans-basin wave trains, GOA MHWs, North Atlantic SSTAs, and ascending motion in key Pacific regions—is distinctly observable in both recent (2013–2016, 2018–2022) and earlier (1949–1952, 1962–1965) multi-year GOA MHW events. Through a combination of observational analyses and climate model experiments, we demonstrate that multi-year MHWs in the GOA are fundamentally trans-basin phenomena, driven by atmospheric wave trains and the feedback loops they generate across the Pacific and Atlantic.

Results

The GOA MHW-inducing trans-basin wave train and its generation

The trans-basin atmospheric wave train associated with MHWs in the GOA is evident from the regression of monthly 200 hPa geopotential height (Z200) anomalies onto a monthly SSTA index averaged over the GOA region (the GOA index; see Methods) for the period 1871–2022 (Fig. 1b). This analysis reveals an atmospheric circulation pattern extending from the Pacific–North America region into the North Atlantic. Embedded within this wave train is an anomalous high-pressure center over the GOA, serving as the primary atmospheric driver of MHWs. The wave train pattern consists of four distinct centers of action: two negative anomalies over the central North Pacific and North America, and two positive anomalies over the northeastern Pacific and along the southeastern coast of North America. The anomaly centers over North America form a north-south dipole structure that extends into the North Atlantic, resembling the Tropical Northern Hemisphere pattern—a key mode of atmospheric variability linking tropical forcing to extratropical circulation[30]. This trans-basin circulation pattern persists year-round, with its structure particularly pronounced during boreal winter (December–February; DJF) (Fig. S1).

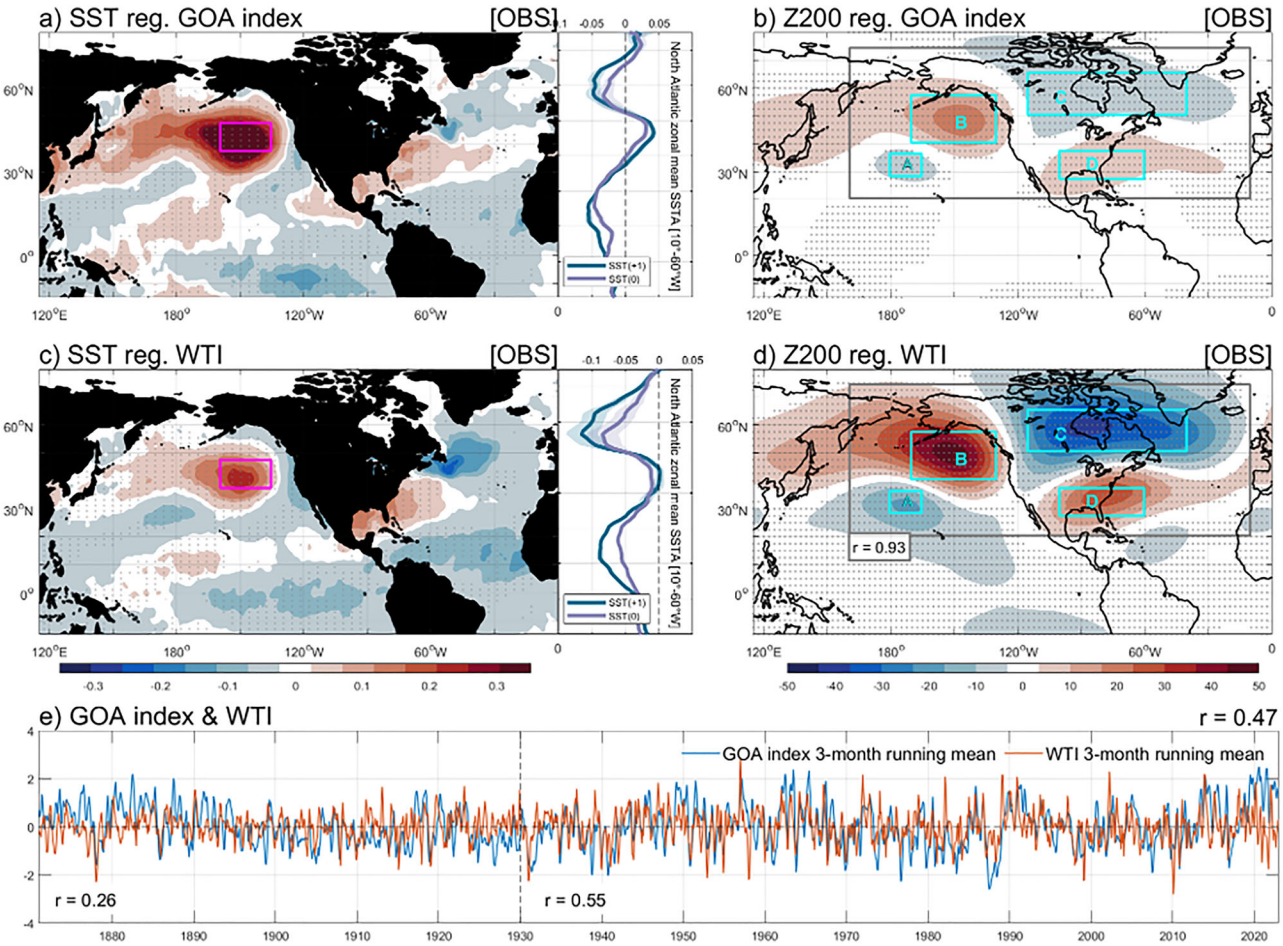

Fig. 1 | Trans-basin Wave Train's Role in Gulf of Alaska Marine Heatwaves. a Left panel: SSTAs regression coefficients (°C) onto the GOA index for the period 1871–2022. Right panel: North Atlantic tripolar SSTA pattern associated with GOA MHWs, showing zonally averaged (10°W–60°W) SSTA regression coefficients onto the GOA index at lag 0 (purple) and lag 1 month (blue). **b** Z200 anomalies regression coefficients (m) onto the GOA index for the period 1871–2022. **c** Same as (**a**) but for the regression onto the WTI. **d** Same as (**b**) but with the WTI. The value 0.93 shown in panel (**d**) represents the pattern correlation between panels (**b**) and (**d**) within the gray box (20°N–75°N, 160°E–10°W). Magenta box shows the GOA region. Cyan boxes (**A**-**D**) mark the four wave train centers. Gray dots in panels (**a**–**d**) indicate significance at the 95% confidence level. **e** The 3-month running mean of the time series of the GOA index (blue) and WTI (orange) during the period 1871–2022. Also shown in the panel are the correlation coefficients between the WTI and the GOA index (lagged by one month): 0.26 for 1871–1929, 0.55 for 1930–2022, and 0.47 for the full period (1871–2022).

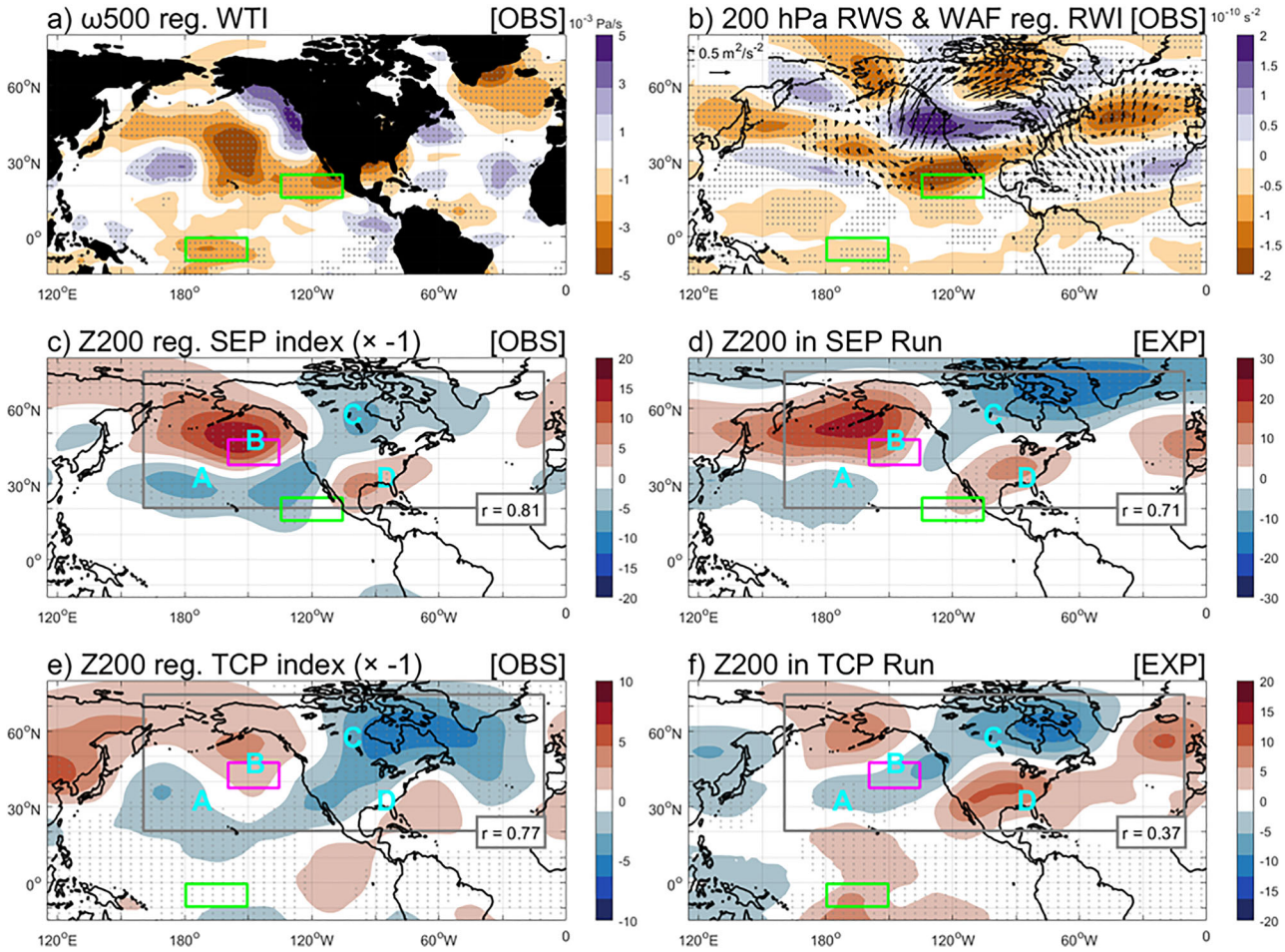

Fig. 2 | Subtropical Eastern Pacific and Tropical Central Pacific Ascending asWave Train Drivers. a Regression coefficients of ω500 (10^{-3} Pa/s) anomalies onto WTI. **b** Regression coefficients of 200hPa RWS (s^{-2}) and WAF (vectors, m^2/s^2) anomalies onto WTI. **c**,**e** Regression of Z200 anomalies onto SEP and TCP indices (multiplied by -1 for visual consistency with SEP/TCP model runs). **d**,**f** Z200 responses in the Forced SEP Run/ TCP Run. Wave train centers **A**-**D** (corresponding to those identified in Fig. 1b) are labeled. GOA region shown by magenta box (**c**–**f**). Green boxes mark SEP region in (**a**–**d**), and TCP region in (**a**,**b**,**e**,**f**). Pattern correlations between panels and Fig. 1b within gray boxes are labeled in (**c**–**f**). Gray dots indicate significance at the 95% confidence level.

To track the activity of trans-basin wave trains, we developed a wave train index (WTI)-based on Z200 anomalies across the four identified centers of action (see Methods). The regression of Z200 anomalies onto the WTI (Fig. 1d) closely mirrors the regression pattern obtained using the GOA index (Fig. 1b), validating the WTI as a reliable metric for capturing the atmospheric forcing responsible for GOA MHWs. The dominant role of the trans-basin wave train is further supported by the strong coherence between the WTI and the GOA index time series over the study period (1871–2022) (Fig. 1e). Notably, this coherence strengthens significantly after 1930, with the correlation between the WTI and the GOA index (lagged by one month to account for oceanic response time, which yields the highest correlation; Fig. S2) increasing from 0.26 during 1871–1930 to 0.55 after 1930. This correlation strengthening after 1930 may reflect improved observational data coverage and quality over time, including the eventual transition to NCEP/NCAR Reanalysis 1 data starting in 1948. However, the temporal evolution of this relationship also suggests that the effectiveness of trans-basin wave trains in driving GOA MHWs may have varied over time, though the underlying causes require further investigation. The correlation remains strong during fall (SON), winter (DJF), and spring (MAM), while slightly weaker yet still significant in summer (JJA; $r = 0.26$, $p < 0.01$), underscoring the year-round influence of trans-basin wave train forcing on GOA MHWs. Regressions of SHF components and surface winds onto the WTI reveal that the trans-basin wave train modulates GOA MHWs primarily through reduced latent heat loss from weakened surface winds (Fig. S3), consistent with previous studies[7].

To identify key regions in the low-latitude Pacific responsible for generating the trans-basin wave train, we regressed anomalies of vertical velocity (ω500) at 500 hPa onto the WTI (Fig. 2a). This analysis highlights two key regions: the tropical central Pacific (TCP; 180°W–150°W, 10°S–0°) and the subtropical eastern Pacific (SEP; 135°W–105°W, 15°N–25°N), where ascending motions show the strongest correlations with the WTI within the low-latitude Pacific (i.e., south of 30°N).

To further investigate the role of these regions in wave train generation, we conducted analyses of the Rossby wave source (RWS) and wave activity flux (WAF) (see Methods). The results reveal significant negative RWS in both TCP and SEP regions (Fig. 2b), indicating strong wave train forcing through convection-induced upper-level divergence. The tropical and subtropical RWS signatures represent primary wave forcing through convective heating and associated upper-level divergence[31], in contrast to mid-latitude RWS patterns that typically reflect secondary effects from wave propagation and interaction with the background atmospheric flow. This distinction is evident in Fig. 2b, where the SEP and TCP regions show coherent negative RWS centers beneath regions of strong upper-level divergence, while mid-latitude RWS patterns appear more fragmented and associated with existing wave features. The SEP exhibits particularly intense forcing due to its optimal positioning beneath the subtropical jet stream, where enhanced divergence interacts with the jet's vorticity gradient,

creating ideal conditions for Rossby wave excitation and propagation. While the TCP region shows weaker RWS values than the SEP region, it represents an established tropical wave source for Northeast Pacific SSTAs[23]. We include both regions for comprehensive coverage of wave generation mechanisms, with the SEP region serving as the primary driver.

The WAF vectors emanating from the SEP region demonstrate clear northeastward energy propagation patterns, with the vectors showing remarkable coherence along the wave train trajectory from the source region to the GOA and extending into the North Atlantic (Fig. 2b). WAF vectors are intentionally omitted in the TCP region because WAF diagnostics become unreliable near the equator. Based on multiple diagnostics (ω500, RWS, WAF), we identify the TCP and SEP regions as the primary wave generation areas within the low-latitude Pacific, showing consistent signatures of atmospheric wave generation and propagation toward the GOA.

Regression analysis of Z200 anomalies onto the TCP and SEP indices of ω500 (see Methods) confirms the wave-generating roles of these regions (Fig. 2c–e). The Z200 patterns regressed onto both indices closely resemble the GOA-regressed wave train structure (Fig. 1b) across the North Pacific–North Atlantic sector (20°N–75°N, 160°E–10°W), with pattern correlations of 0.77 ($p < 0.01$) for the TCP and 0.81 ($p < 0.01$) for the SEP. Notably, the SEP-regressed wave train exhibits remarkable spatial and amplitude consistency throughout the year, highlighting its dominant role in wave train generation. In contrast, the TCP-regressed pattern shows pronounced seasonal variability, with peak correlations observed during spring and summer (Fig. S4).

To further evaluate the contributions of the TCP and SEP regions to trans-basin wave train excitation, we conducted idealized forcing experiments using the Community Atmospheric Model version 5 (CAM5). We prescribed positive SSTAs in the SEP and TCP regions to simulate negative ω500 anomalies (see Methods), successfully reproducing the observed wave train patterns (Fig. 2d, f). The SEP Run (Fig. 2d) generated a wave train structure nearly identical to that observed (Figs. 2c, 1b), with well-defined anomaly centers matching both in location and amplitude. The TCP Run (Fig. 2f) also produced a coherent wave train, though with the high-pressure anomaly slightly displaced northward relative to the observed GOA center, and with a weaker overall pattern correlation compared to the SEP Run. This suggests that while the TCP region can generate relevant wave trains, the SEP region is the more robust and consistent driver of GOA-affecting wave patterns. The seasonal dependence of wave train excitation in these experiments mirrors the seasonal variability observed in the regression analyses with the TCP and SEP indices (Fig. S4). Together, these experiments provide robust evidence that ascending motions over the TCP and SEP regions are key drivers of trans-basin atmospheric wave trains linked to GOA MHWs, with the TCP region playing a secondary and more variable role.

Atlantic SST responses to trans-basin wave trains and their feedback on the Pacific

Since the trans-basin atmospheric wave train that drives GOA MHWs extends across ocean basins, it also influences SSTAs in the North Atlantic, as shown by the SSTAs regression onto the WTI in Fig. 1c. This regression reveals that, alongside GOA warming during MHW events, a characteristic tripolar SSTA pattern emerges in the North Atlantic. This pattern—more clearly depicted in the zonal mean of SSTAs across the Atlantic Basin—becomes even more pronounced one month following the wave train (Fig. 1c). The tripolar pattern is characterized by cooling in the subpolar (40°N–60°N) and subtropical (0°N–25°N) regions, along with warming in the mid-latitudes (25°N–40°N). A similar Pacific–Atlantic SSTAs linkage during GOA MHWs is evident in the SSTAs regression onto the GOA index (Fig. 1a). Previous work[7] suggested that this tripolar SSTA pattern in the North Atlantic is generated by the trans-basin atmospheric wave train through its modulation of the Atlantic tropospheric jet stream and associated SHF anomalies[32–34].

Among the three SSTA centers of the tripolar pattern, the Tropical Northern Atlantic (TNA) has been shown to exert significant feedback on Pacific climate variability through atmospheric teleconnections, as documented in previous studies on trans-basin interactions[26,35]. To explore the potential feedback of TNA cooling on the Pacific, we regressed ω500 and 200 hPa divergent wind (UV_d200) anomalies onto the TNA index (see Methods). The regression results reveal that TNA SST cooling is associated with anomalous descending motion over the TNA region, accompanied by corresponding ascending motion over the SEP and TCP regions (Fig. 3a). These regions are linked by anomalous upper-level divergent winds, with UV_d200 diverging from the SEP and TCP regions and converging into the TNA region.

To further confirm the causal relationship between TNA SST cooling and ascending motion over the SEP and TCP regions, we conducted a forced TNA experiment using the CAM5 model, where an idealized Gaussian-shaped SST cooling was prescribed in the TNA region (see Methods). This TNA Run successfully reproduced the observed regression patterns (cf. Fig. 3a, b), demonstrating that TNA cooling induces local descending motion, which in turn generates upper-level convergence. This convergence draws divergent winds from the SEP and TCP regions, promoting ascending motion in these key Pacific areas.

To investigate the underlying feedback pathways, we performed vertical cross-section analyses along the subtropical (15°N–25°N) and equatorial (10°S–0°) bands of the Pacific–Atlantic Ocean in the model experiment. The analysis reveals that TNA cooling influences zonal overturning circulation patterns across both bands. Specifically, TNA cooling directly induces anomalous descending motion in the 90°W–30°W sector of the subtropical band, accompanied by anomalous ascending motion over the SEP region (Fig. 3d). The descending motion in the TNA region also draws air from the equatorial band, driving anomalous ascending motion in the equatorial Atlantic within the same longitudinal sector (Fig. 3f). This equatorial ascending motion initiates a sequence of overturning circulations, resulting in descending motion in the equatorial eastern Pacific sector (100°W–80°W) and generating subsequent overturning circulation that elevates air over the TCP region. Observational regression analyses (Fig. 3c, e) corroborate these model findings, with particularly robust connectivity observed in the subtropical band compared to the equatorial band. The relatively weaker observational signals in the equatorial band may reflect the influence of El Niño–Southern Oscillation (ENSO), which can modulate the impact of TNA SSTAs in observations but is absent in the idealized model experiments.

Since TNA SST cooling can feedback to trigger ascending motion over the SEP and TCP regions, it is expected to reactivate the trans-basin wave train that drives GOA MHWs. This hypothesis is supported by the regression of Z200 anomalies onto the TNA index in both observations and the TNA Run, each producing trans-basin structures that closely resemble the observed trans-basin wave train pattern (Fig. S5). The resemblance is particularly strong in the TNA Run compared to the observational regression, likely due to the absence of confounding climate variability in the model. The strong structural similarity between the modeled and observed wave train patterns provides compelling evidence that TNA cooling can indeed reactivate the trans-basin wave train responsible for driving GOA MHWs.

Our observation analyzes and forced model experiments together reveal that multi-year GOA MHWs can be explained as a trans-basin interaction phenomenon sustained through a self-reinforcing feedback loop between the North Pacific and North Atlantic. Fig. 4 presents a schematic illustration summarizing the key processes involved in this mechanism, which unfolds as follows:

(1) Anomalous ascending motion over TCP and SEP (steps 1a and 1b in Fig. 4) initiates the trans-basin wave train (step 2 in Fig. 4).
(2) This wave train triggers a GOA MHW episode primarily through SHF forcing (step 2 in Fig. 4).
(3) The wave train propagates into the North Atlantic, inducing tripolar SSTA pattern (step 3 in Fig. 4).
(4) Cooling in the TNA region promotes anomalous ascending motion over TCP and SEP regions (steps 4a and 4b).

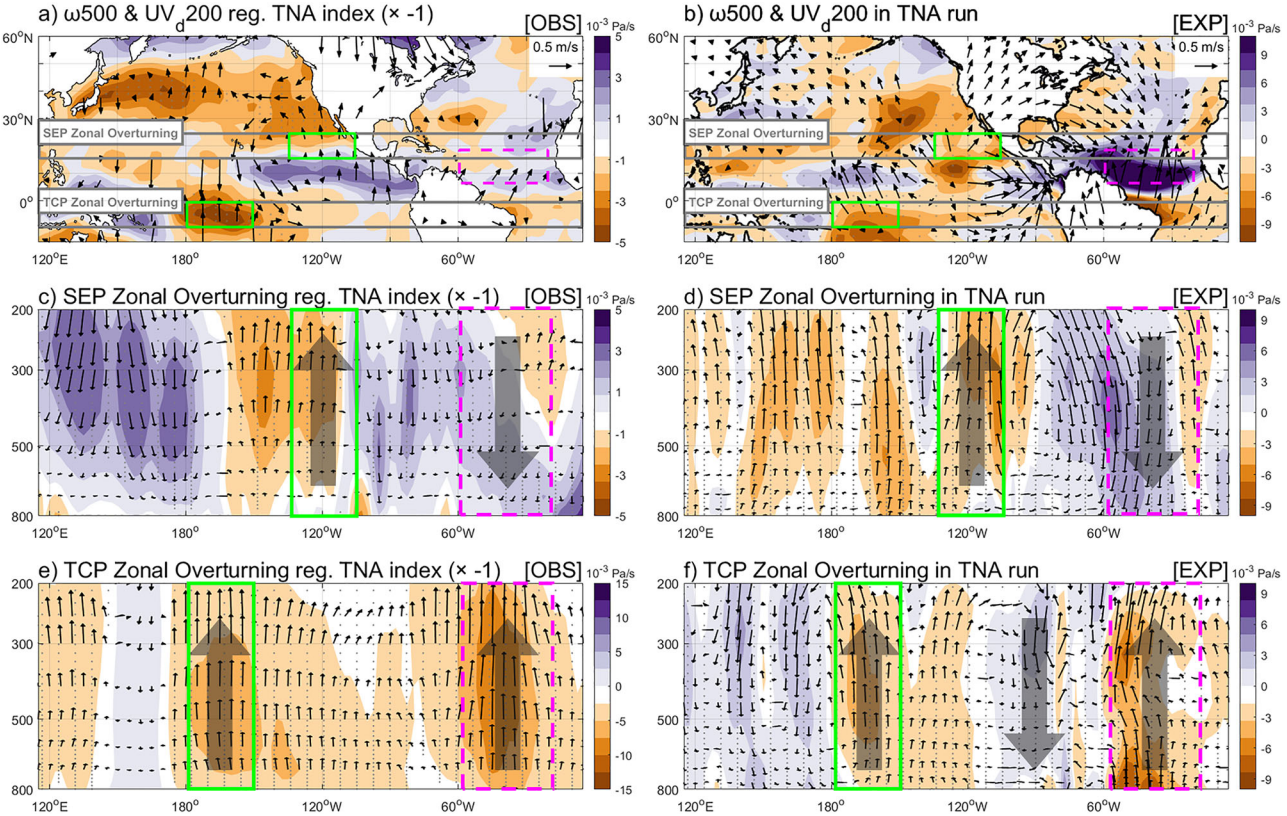

Fig. 3 | Tropical Northern Atlantic Cooling Impact on TCP/SEP Ascending through Zonal Circulation. a ω500 (shading, 10^{-3} Pa/s) and UV_d200 (vectors, m/s) regression onto TNA index (multiplied by -1 for visual consistency with TNA model run). **b** ω500 and UV_d200 responses in the Forced TNA Run. **c**, **e** Vertical velocity (omega; shading, 10^{-3} Pa/s) regression onto TNA index along SEP/TCP latitude bands (multiplied by -1 for visual consistency with TNA model run). **d**, **f** Omega responses in the TNA Run along SEP/TCP regions. Green boxes mark: SEP region in (**c**, **d**) and TCP region in (**e**, **f**). Magenta box marks TNA region. Gray boxes indicate latitude bands used for cross-section analysis. Gray dots indicate significance at the 95% confidence level.

(5) A new wave train sequence is generated, initiating another GOA MHW episode.

This trans-basin interaction loop (steps 1–4 in Fig. 4) can produce consecutive MHW episodes in the GOA region, giving rise to multi-year MHW events. The feedback loop persists until it is interrupted by other climate variability modes or internal variability within the Pacific or Atlantic Oceans.

To further confirm the causal relationships within this feedback loop, we performed a multivariate Granger Causality (GC) analysis (see Methods). This method identifies causal relationships by testing whether past values of one variable X can predict future changes in another variable Y employing vector autoregression models[36,37] and is well-suited for analyzing causal relationships in interacting climate systems[38,39]. A statistically significant ($p < 0.05$) causal pathway is denoted as "X → Y" when variable X shows predictive influence on variable Y.

We analyzed five key components of the feedback loop (Fig. 4): ascending motion in the TCP and SEP regions (TCP and SEP indices), the trans-basin wave train (WTI), GOA warming (GOA index), and tropical North Atlantic cooling (TNA index). Using time series for these indices over the period 1871–2022, our GC analysis results (Table S1 and Fig. S6) reveal a primary feedback loop with the following causal sequence: SEP → WTI → TNA → SEP and TCP. This pathway validates the self-reinforcing feedback mechanism depicted in Fig. 4. Additionally, the GC analysis reveals that a statistically significant causal relationship also exists between the WTI and the GOA index, with the WTI driving the GOA SST warming, confirming that the trans-basin wave trains drive MHWs in the GOA region. Given the potential nonlinear nature of ocean-atmosphere interactions, we further validated our findings using Convergent Cross Mapping (CCM), which is specifically designed for nonlinear dynamical systems and has been successfully applied to climate teleconnections[38]. CCM detects causation through increasing predictive skill as more data becomes available (see Methods). The CCM results (Fig. S7) largely support the key causal relationships identified by GC, providing robust validation of our trans-basin feedback mechanism using a nonlinear approach.

Evidence of trans-basin feedback loops in historical multi-year GOA MHW events

To further demonstrate that the trans-basin feedback loop is responsible for sustaining multi-year GOA MHWs, we analyzed four historical events to determine whether the key elements of this feedback mechanism can be identified. Specifically, we compared two recent events (2013–2016 and 2018–2022) with two earlier events (1949–1952 and 1962–1965) to examine whether the trans-basin feedback operates similarly across different climate periods.

During the 2013–2016 multi-year MHW event, we identified four distinct wave train episodes based on positive WTI values (Fig. 5a, black line). Throughout these episodes (highlighted by gray shading in Fig. 5a–c), a pattern of negative-positive-negative-positive Z200 anomalies emerged (Fig. 5a, left panel), reflecting the trans-basin wave train structure (cf. Fig. 1b). This pattern extended from the subtropical North Pacific (centered around 175°W, 32°N) toward the GOA in the northeastern Pacific, continuing over northern North America (centered around 100°W, 55°N), and then turning equatorward into the Atlantic Ocean (centered around 85°W, 35°N). During each episode, the wave trains generated anomalous high-pressure systems over the GOA, leading to significant SST warming (Fig. 5b, left panel). The GOA index (Fig. 5b, red line in the right panel) exceeded the MHW threshold (Fig. 5b, blue line) approximately 1–2 months after each wave train episode. This sequence resulted in three major MHW events:

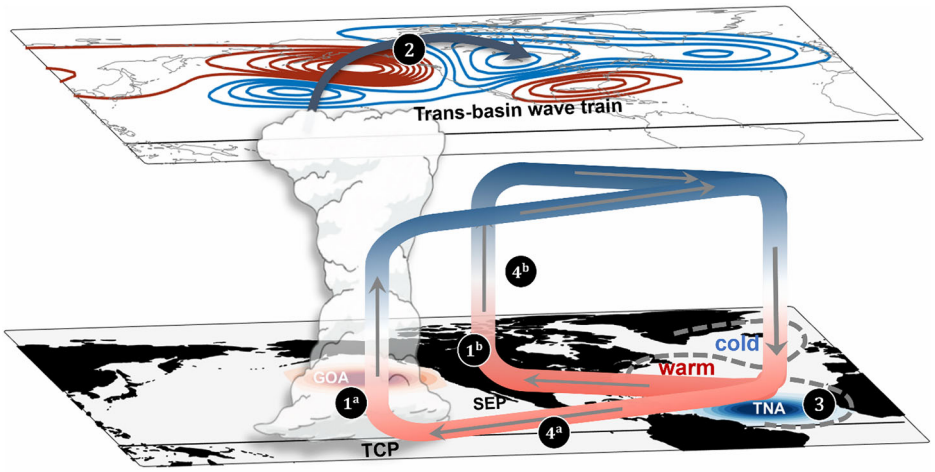

Fig. 4 | Self-reinforcing feedback loop between Pacific and Atlantic driving GOA Marine Heatwaves. (1) Ascending air motions in the Tropical Central Pacific (1a) and Subtropical Eastern Pacific (1b) generate the trans-basin atmospheric wave train (2), which drives both Gulf of Alaska Marine Heatwaves and Tropical North Atlantic cooling (3). The resulting TNA cooling then triggers new ascending motions in the TCP (4a) and SEP (4b) regions, completing and sustaining the cycle.

April–August 2013, November 2013–September 2014, and February–September 2015, with an additional event from June–August 2016. While this fourth event does not meet the duration criterion for MHWs (see Methods), its occurrence supports the hypothesis that each wave train episode during 2013–2016 contributed to distinct GOA warming events. TNA SST cooling was observed during the latter three of the four wave train episodes (Fig. 5c, left panel), with particularly evident cooling during the second and third episodes, while the fourth episode showed weaker cooling located further east of the TNA region. Analysis of the TCP and SEP ω500 indices revealed that the SEP region exhibited a more consistent response to TNA cooling, as indicated by positive SEP index values (Fig. 5c, blue line), reflecting anomalous ascending motion. In contrast, the TCP region showed significant ascending motion only during the third wave train episode (Fig. 5c, green line), coinciding with the development of the 2015–2016 El Niño (Fig. 5d).

For the 2018–2022 GOA MHW, we conducted a similar analysis and identified five wave train episodes based on the WTI (Fig. 5e, black line) and corresponding positive Z200 anomalies over the GOA region (Fig. 5e, left panel). All five wave train episodes were associated with significant GOA SST warming (Fig. 5f, left panel) and TNA SST cooling (Fig. 5g, left panel). Except for the first episode, the GOA index during the remaining four episodes (Fig. 5f, red line in the right panel) exceeded the 90th percentile threshold (Fig. 5f, blue line), qualifying them as MHW events. Positive SEP index values were observed during three of the five wave train episodes, with the exceptions occurring during the third and fourth episodes (Fig. 5g, blue line in the right panel). Notably, these two episodes coincided with the prolonged La Niña event from 2020 to 2022 (Fig. 5h). La Niña typically excites wave trains resembling the negative Pacific–North American pattern, which may have suppressed ascending motion over the SEP region, potentially explaining the absence of positive SEP index values during these episodes. Additionally, ascending motion over the TCP region was also absent during these two episodes, suggesting that other factors beyond SEP and TCP ascending may contribute to trans-basin wave train excitation—an area warranting further investigation. Nevertheless, the key elements of the self-reinforcing feedback loop are evident in most episodes of the 2018–2022 multi-year GOA MHWs.

Analyses of the two earlier historical events (1949–1952 and 1962–1965) also align with the trans-basin interaction framework. The 1949–1952 event exhibited five distinct wave train episodes (Fig. 5i–l), while the 1962–1965 event showed three wave train episodes (Fig. 5m–p). GOA warming, TNA cooling, and SEP-associated ascending motion were evident in the majority of these episodes. Interestingly, we observed an increased occurrence of positive TCP index values—indicative of enhanced ascending motion over the TCP region—during the wave train episodes of these earlier events. This suggests that the relative importance of ascending motion in the TCP versus SEP regions may have shifted over time, with TCP playing a more prominent role in earlier multi-year GOA MHWs compared to recent events.

Across all four historical MHW events, we observed varying ENSO conditions: the 2013–2016 MHW overlapped with the 2014–2015 El Niño, the 2018–2022 MHW coincided with the 2020–2022 La Niña, the 1949–1952 event spanned a transition from La Niña to El Niño, and the 1962–1965 event experienced fluctuating ENSO phases (Fig. 5). The occurrence of multi-year GOA MHWs across diverse ENSO conditions suggests that these events are not primarily driven by ENSO, further highlighting the critical role of the trans-basin feedback mechanism outlined in this study.

Discussion

This study investigates the dynamics underlying multi-year MHWs in the GOA, with a focus on the roles of atmospheric wave trains and trans-basin interactions. Our findings indicate that multi-year GOA MHWs are not isolated Northeastern Pacific events but are instead trans-basin phenomena sustained through continuous interactions between the Pacific and Atlantic basins. This shift in perspective highlights the critical role of trans-basin connections in sustaining prolonged marine heatwave conditions.

By framing MHWs within the context of trans-basin atmospheric wave trains, this study underscores the importance of revisiting atmospheric wave dynamics, particularly trans-basin stationary waves. Although atmospheric wave trains were extensively studied from the 1970s to the 1990s[40–45], their trans-basin characteristics have received considerably less attention. Recent modeling work by O'Brien and Deser[46] suggests that anthropogenic climate forcing has altered atmospheric circulation patterns, expanding the spatial reach of key extratropical modes. While the implications for trans-basin interactions require further investigation, studies documenting Atlantic-Pacific connections[47] suggest that such interactions may play an increasingly important role in the climate system.

Notably, O'Brien and Deser's[46] results show a shift in the leading mode of boreal winter geopotential height at 500 hPa—from the Pacific–North American pattern during 1923–1933 to a trans-basin wave train pattern projected for the late 21st century (2088–2099). This projected pattern closely resembles the trans-basin wave train structure identified in our study (Fig. 1b) that drives GOA MHWs. These findings imply that global warming may promote the dominance of trans-basin stationary waves in the extratropical atmosphere, potentially increasing the persistence and intensity of extreme climate events, such as multi-year GOA MHWs.

Furthermore, our results indicate that Atlantic SSTA conditions could serve as early warning indicators for prolonged GOA MHW events, highlighting the need for integrated monitoring of both the Pacific and Atlantic basins to improve forecasting capabilities. However, multiple factors can modulate or disrupt this trans-basin feedback loop, adding complexity to prediction efforts. For example, ENSO activity in the tropical Pacific may

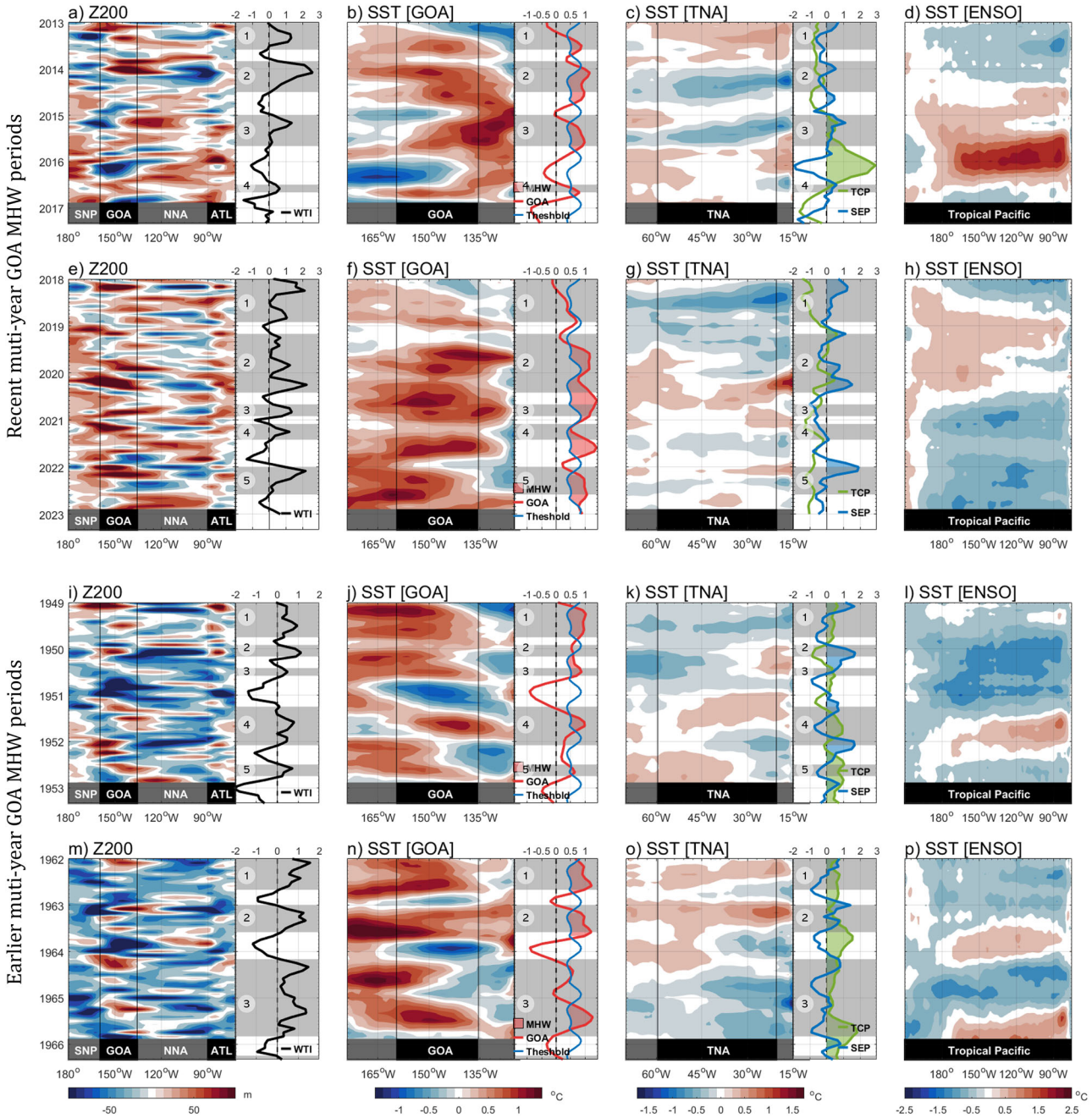

Fig. 5 | Historical wave train episodes sustaining multi-year Gulf of Alaska Marine Heatwaves. Time evolution during four major multi-year MHW events: 2013–16 (**a–d**), 2018–22 (**e–h**), 1949–52 (**i–l**), and 1962–65 (**m–p**). For each event: first column shows Z200 anomalies along the wave train track at four key centers of action—SNP (Subtropical North Pacific), GOA (Gulf of Alaska), NNA (Northern North America), and ATL (North Atlantic) (see Fig. S9); second column shows GOA SSTA (37.5°N–47.5°N); third column shows TNA SSTA (6.5°N–18.5°N); fourth column shows ENSO region SSTA (10°S–10°N). The corresponding climate indices are shown to the right of these evolution panels. Gray shading marks WTI > 0 episodes, with episode numbers labeled. A 3-month running mean was applied to all values. The TCP and SEP index values have been multiplied by −1 for visual clarity, positive (negative) values represent ascending (descending) motion here.

compete for influence over ascending or descending motions in the TCP and SEP regions, potentially interrupting the continuous triggering of trans-basin wave trains by TNA cooling. Additionally, intrinsic atmospheric variability, such as the North Atlantic Oscillation, can interfere with the proposed mechanism, either amplifying or dampening the feedback loop.

Our findings demonstrate that multi-year GOA MHWs represent a distinct class of trans-basin interaction phenomena, sustained by self-reinforcing feedback loops between Pacific and Atlantic SSTs. This mechanistic understanding offers insights that may contribute to improving early warning systems through integrated Pacific-Atlantic monitoring and enhance our ability to predict the duration and intensity of these economically and ecologically significant climate events.

Methods

Observational data

This study covers the period from 1871 to 2022. Monthly sea surface temperature (SST) data at 1° × 1° spatial resolution were obtained from the Hadley Center Sea Ice and SST dataset[48]. Atmospheric variables, including monthly mean geopotential height at 200 hPa (Z200), vertical velocity, Surface Heat Flux (SHF; including latent heat, sensible heat, shortwave

radiation, and longwave radiation), sea level pressure (SLP), surface wind (UVsfc), and 200 hPa divergent wind (UV_d200), were sourced from two datasets. The 20th Century Reanalysis V2[49] provided data for 1871–1947, while the NCEP/NCAR Reanalysis 1[50] covered 1948–2022. Monthly anomalies for atmospheric variables were computed by combining data from these sources. The 20th Century Reanalysis V2 has a spatial resolution of 2° × 2°, while NCEP/NCAR Reanalysis 1 has 2.5° × 2.5° resolution. The 20th Century Reanalysis V2 dataset was cubic interpolated to the 2.5°×2.5° grid for consistency. For both ocean and atmospheric variables, anomalies were calculated as deviations from the 1981–2010 seasonal cycle average, a standard baseline period commonly used in climate studies, with linear trends removed. Sensitivity analysis using NCEP-DOE Reanalysis 2[51] for 1979–2022 confirmed key correlations remain robust (WTI-GOA: NCEP-2 $r = 0.544$ vs NCEP-1 $r = 0.545$; WTI inter-dataset: $r = 0.999$), validating our results are not dependent on the specific reanalysis dataset.

MHW Definition and the GOA Index

The GOA index is defined as the SSTA averaged over 160°W–135°W, 37.5°N–47.5°N, and is normalized. The identification of MHWs in the GOA region follows the criteria established by Hobday et al.[52] and Zhao and Yu[7]. An MHW event is defined as a period during which the monthly GOA index exceeds its 90th percentile threshold for a minimum of five consecutive months. The threshold values are calculated using the 1981–2010 baseline period to account for seasonal variability. To address temporal continuity, events separated by a single month are merged into one event, ensuring robust identification of persistent warming anomalies.

We define a multi-year MHW period as any time when MHWs occur in at least three out of four consecutive years (see Table S3). From these periods, we selected four for detailed analysis: 1949–1952, 1962–1965, 2013–2016, and 2019–2022. We focused on these more recent periods due to the availability of higher-quality observational data.

Trans-basin atmospheric wave train episode and the WTI

The WTI is used to quantify the strength of trans-basin atmospheric wave trains across the North Pacific–North Atlantic sector. This approach adapts established methods for creating circulation indices based on key centers of action[41], where indices are constructed by averaging normalized height anomalies at identified centers. The WTI is defined as the average of Z200 anomalies at two positive anomaly centers—Region B (170°W–130°W, 40.5°N–57.5°N) and Region D (100°W–60°W, 27.5°N–37.5°N)—minus the average of Z200 anomalies at two negative anomaly centers—Region A (180°–165°W, 28.5°N–36.5°N) and Region C (125°W–40°W, 50.5°N–65.5°N), and is normalized (illustrated in Fig. 1b). These wave train centers were identified based on the spatial pattern revealed through linear regression analysis of Z200 anomalies onto the GOA index. A trans-basin wave train episode is defined as a period when the WTI is greater than zero ($WTI > 0$).

Other climate indices

To identify wave train source regions, we defined two indices based on ω500 anomalies. The Subtropical Eastern Pacific (SEP) Index represents the average ω500 anomalies within the region 135°W–105°W, 15°N–25°N, while the Tropical Central Pacific (TCP) Index covers 180°W–150°W, 10°S–0°, (illustrated in Fig. 2a). Both indices are normalized, with negative values representing ascending motion (upward vertical velocity that promotes convection and atmospheric wave generation through upper-level divergence), while positive values represent descending motion.

The Tropical North Atlantic (TNA) index is used to quantify the magnitude of SSTAs in the TNA region, defined as the average SSTAs between 20°W–60°W and 6.5°N–18.5°N, and is normalized.

Wave Activity Diagnostics: RWS and WAF

The RWS, derived from the barotropic vorticity equation in pressure coordinates, quantifies wave generation through the interaction between divergent flow and absolute vorticity[31]:

$$RWS = -\nabla\cdot(v_\chi\zeta_a) - \zeta_a\nabla\cdot v_\chi \tag{1}$$

where the divergence operator is defined as $\nabla\cdot v = (\partial u/\partial x + \partial v/\partial y)$, where u and v are zonal and meridional wind components. v_χ is the divergent component of the wind, and ζ_a is the absolute vorticity, calculated as:

$$\zeta_a = \zeta_r + f \tag{2}$$

where relative vorticity $\zeta_r = \partial v/\partial x - \partial u/\partial y$ and planetary vorticity $f = 2\Omega\sin(\varphi)$, with Ω being Earth's rotation rate and φ the latitude. The results obtained using monthly wind data are very similar to those obtained using daily data when analyzing the seasonal scale of the RWS computed at 200 hPa[53]. Monthly data are used in this study.

The 200 hPa WAF was calculated following the method described by Takaya and Nakamura[54], which is expressed by the following equation:

$$W = \frac{pcos\varphi}{2|UV|}\begin{bmatrix} \frac{U}{a^2cos^2\varphi}\left[\left(\frac{\partial\psi'}{\partial\lambda}\right)^2 - \psi'\frac{\partial^2\psi'}{\partial\lambda^2}\right] + \frac{V}{a^2cos\varphi}\left(\frac{\partial\psi'}{\partial\lambda}\frac{\partial\psi'}{\partial\varphi} - \psi'\frac{\partial^2\psi'}{\partial\lambda\partial\varphi}\right) \\ \frac{U}{a^2cos\varphi}\left(\frac{\partial\psi'}{\partial\lambda}\frac{\partial\psi'}{\partial\varphi} - \psi'\frac{\partial^2\psi'}{\partial\lambda\partial\varphi}\right) + \frac{V}{a^2}\left[\left(\frac{\partial\psi'}{\partial\varphi}\right)^2 - \frac{\psi'\partial^2\psi'}{\partial\varphi^2}\right] \end{bmatrix} \tag{3}$$

In Eq. (3), W represents the WAF vector, p is pressure divided by 1000 hPa, φ is latitude, UV is the background wind vector (U, V), a is Earth's radius, ψ' is the perturbation stream function, and λ is longitude. WAF is a quantitative diagnostic tool for identifying the propagation of stationary Rossby waves in the upper troposphere[54,55].

These calculations provide insights into the generation and propagation of large-scale atmospheric waves.

Forced Atmospheric General Circulation Model (AGCM) Experiments

We performed forced AGCM experiments using the F-1850 compset of CAM5[56], configured with a horizontal resolution of ~2.5° longitude × 1.9° latitude and 30 vertical layers extending from the surface to 3.65 hPa. Four experiments were conducted: the control (CTRL) Run, along with three sensitivity runs (TCP, SEP, and TNA). In the CTRL Run, monthly varying climatological SST and sea ice[57] (Fig. S8a) were prescribed to drive CAM5. The TCP and SEP Runs explored whether negative ω500 anomalies in these respective regions could produce atmospheric wave trains akin to those observed during GOA MHWs, by imposing an idealized 2 °C Gaussian-shaped SST anomaly in each region (Fig. S8b, c) to simulate anomalous upward motion. For the TNA Run, we added a Gaussian-shaped SST anomaly (−2 °C peak intensity) to the monthly varying SST climatology over the TNA region (Fig. S8d), enabling an assessment of how TNA SST cooling influences atmospheric circulation. Each experiment was integrated for 25 years, with the final 20 years used for analysis. The differences between the TCP, SEP, and TNA Runs and the CTRL Run are defined as the atmospheric responses to the prescribed SST anomaly forcing and are analyzed in detail in this study.

GC Test

To systematically evaluate the proposed Pacific-Atlantic interaction loop, we implemented multivariate GC tests using vector autoregression (VAR) model[36,37]. The VAR model framework is defined as:

$$Y(t) = \alpha_0 + \sum_{i=1}^{p}\alpha(i)Y(t-i) + \sum_{i=1}^{p}\beta(i)X(t-i) + \varepsilon(t) \tag{4}$$

In Eq. (4), $Y(t)$ is the dependent variable at time t, $Y(t\text{-}i)$ represents the lagged (past) values of the dependent variable Y itself, $X(t\text{-}i)$ represents

lagged values of the predictor variable, α_0 is the intercept term, $\alpha(i)$ and $\beta(i)$ are the regression coefficients that quantify the influence of past values on the current state, p is the lag order, and $\epsilon(t)$ is the error term. The GC test evaluates whether past values of X (e.g., SEP index) significantly improve predictions of Y (e.g., WTI) beyond the explanatory power of Y's own history. Formally, the null hypothesis ($H0$: $\beta(i)=0$ *for all* i) posits that X does not Granger-cause Y. Rejection of $H0$ implies that X contains unique predictive information for Y, revealing direct or indirect causal pathways within the coupled system. We applied this framework to monthly indices (SEP, TCP, WTI, GOA, and TNA) spanning 1871–2022, constructing a 5-variable VAR model where each variable is regressed on its own lagged values plus lagged values of all other variables in the system. Among the different lag orders tested (1–12 months), a lag of six months was identified as optimal by the Akaike Information Criterion[58], which balances model fit against complexity by penalizing excessive parameters. Sensitivity analysis using lag orders 4–8 months confirmed that the core causal relationships (SEP → WTI → GOA and TNA → SEP) remain statistically significant, ensuring our conclusions are robust to lag choice (Table S2).

CCM analysis

To address potential nonlinear relationships in our causal analysis, we implemented Convergent Cross Mapping (CCM) following[59]. CCM tests for causation by examining whether the historical values of variable X can predict variable Y in a nonlinear dynamical system. Unlike GC, CCM does not assume linear relationships and can detect causation in deterministic nonlinear systems where variables are synchronized. We used embedding dimension E = 6, time delay $\tau = 1$, and 7 nearest neighbors for prediction, with library sizes ranging from 20–150 points in increments of 5. Convergent behavior—characterized by increasing ρ values with larger library size—indicates genuine causal relationships in climate systems and has been successfully applied to climate teleconnections. We applied CCM to the same monthly indices used in GC analysis (SEP, TCP, WTI, GOA, and TNA) for the period 1871–2022.

Regression methods

Linear regression analyses were performed between normalized climate indices and gridded anomaly fields using least-squares fitting. We calculated Pearson correlation coefficients between index time series and local anomaly values at each grid point. Pattern correlations between different regression maps were calculated as spatial correlation coefficients within specified domains (indicated by gray boxes in figures). All regression results shown represent regression coefficients, indicating the typical anomaly pattern associated with a one-standard-deviation change in the respective index. This spatial regression approach differs from the VAR models used for GC testing, which employ lagged temporal relationships between time series.

Statistical significance test

For correlation and regression coefficients, statistical significance was assessed using Student's t-test. In GC tests, we assessed whether the combined lagged effects of the predictor variable were statistically significant using chi-square tests.

Data availability

All data generated during the study are publicly available. The Hadley Center Sea Ice and SST data are available at https://www.metoffice.gov.uk/hadobs/hadisst/. The National Centers for Environmental Prediction/National Center for Atmospheric Research Reanalysis 1 data are available at https://psl.noaa.gov/data/gridded/data.ncep.reanalysis.html. The NCEP-DOE Reanalysis 2 data are available at https://psl.noaa.gov/data/gridded/data.ncep.reanalysis2.html. The Twentieth Century Reanalysis Project dataset is available at https://psl.noaa.gov/data/gridded/data.20thC_ReanV2.html. The Community Atmosphere Model version 5 (CAM5) used for the forced mode experiments is freely available as part of the Community Earth System Model (CESM) project. It can be obtained from the National Center for Atmospheric Research (NCAR) website (https://www2.cesm.ucar.edu/models/cesm1.1/). The idealized CAM5 SST forcing simulations data used in this study can be obtained by contacting Y. Zhao at yzhao@uci.edu.

Code availability

The codes used to generate all the main figures in this study have been archived in the Zenodo database under the accession code https://zenodo.org/record/11640910, or they can be obtained upon request from the author, Y. Zhao.

Received: 1 May 2025; Accepted: 29 July 2025;
Published online: 08 August 2025

References

1. Bond, N. A., Cronin, M. F., Freeland, H. & Mantua, N. Causes and impacts of the 2014 warm anomaly in the NE Pacific. *Geophys. Res. Lett.* **42**, 3414–3420 (2015).
2. Di Lorenzo, E. & Mantua, N. Multi-year persistence of the 2014/15 North Pacific marine heatwave. *Nat. Clim. Change.* **6**, 1042–1047 (2016).
3. Hobday, A. J. et al. Categorizing and naming marine heatwaves. *Oceanography.* **31**, 162–173 (2018).
4. Oliver, E. C. et al. Projected marine heatwaves in the 21st century and the potential for ecological impact. *Front. Mar. Sci.* **6**, 734 (2019).
5. Holbrook, N. J. et al. Keeping pace with marine heatwaves. *Nat. Rev. Earth Environ.* **1**, 482–493 (2020).
6. Amaya, D. J. et al. Are long-term changes in mixed layer depth influencing North Pacific marine heatwaves? *Bull. Am. Meteorol. Soc.* **102**, S59–S66 (2021).
7. Zhao, Y. & Yu, J.-Y. Two marine heatwave (MHW) variants under a basinwide MHW conditioning mode in the North Pacific and their Atlantic Associations. *J. Clim.* **36**, 8657–8674 (2023).
8. Hu, Z.-Z., McPhaden, M. J., Huang, B., Zhu, J. & Liu, Y. Accelerated warming in the North Pacific since 2013. *Nat. Clim. Change* **14**, 929–931 (2024).
9. Hu, Z.-Z., Kumar, A., Jha, B., Zhu, J. & Huang, B. Persistence and predictions of the remarkable warm anomaly in the northeastern Pacific Ocean during 2014–16. *J. Clim.* **30**, 689–702 (2017).
10. Chen, Z., Shi, J., Liu, Q., Chen, H. & Li, C. A persistent and intense marine heatwave in the Northeast Pacific during 2019–2020. *Geophys. Res. Lett.* **48**, e2021GL093239 (2021).
11. Whitney, F. A. Anomalous winter winds decrease 2014 transition zone productivity in the NE Pacific. *Geophys. Res. Lett.* **42**, 428–431 (2015).
12. Peterson, W., Robert, M. & Bond, N. The warm blob continues to dominate the ecosystem of the northern California current. *PICES Press.* **23**, 44 (2015).
13. Frölicher, T. L. & Laufkötter, C. Emerging risks from marine heat waves. *Nat. Commun.* **9**, 650 (2018).
14. Biela, V. R. et al. Premature mortality observations among Alaska's Pacific Salmon during record heat and drought in 2019. *Fisheries.* **47**, 157–168 (2022).
15. Gomes, D. G. et al. Marine heatwaves disrupt ecosystem structure and function via altered food webs and energy flux. *Nat. Commun.* **15**, 1988 (2024).
16. Smith, K. E. et al. Ocean extremes as a stress test for marine ecosystems and society. *Nat. Clim. Change.* **15**, 231–235 (2025).
17. Swain, D. L. et al. The extraordinary California drought of 2013/2014: character, context, and the role of climate change. *Bull. Am. Meteorol. Soc.* **95**, S3 (2014).
18. Amaya, D. J., Miller, A. J., Xie, S.-P. & Kosaka, Y. Physical drivers of the summer 2019 North Pacific marine heatwave. *Nat. Commun.* **11**, 1903 (2020).
19. Ge, Z.-A., Chen, L., Li, T. & Sun, M. Unraveling the formation mechanism of exceptionally strong marine heatwaves in the Northeast Pacific in 2020. *J. Clim.* **36**, 8091–8111 (2023).

20. Giese, B. S. & Carton, J. A. The seasonal cycle in coupled ocean-atmosphere model. *J. Clim* **7**, 1208–1217 (1994).
21. Fedorov, A. V. Ocean-atmosphere coupling. *Oxf. Companion Glob. Change.* **369**, 374 (2008).
22. Liang, Y.-C., Yu, J.-Y., Saltzman, E. S. & Wang, F. Linking the tropical Northern Hemisphere pattern to the Pacific warm blob and Atlantic cold blob. *J. Clim.* **30**, 9041–9057 (2017).
23. Hong, H.-J. & Hsu, H.-H. Remote tropical central Pacific influence on driving sea surface temperature variability in the Northeast Pacific. *Environ. Res. Lett.* **18**, 044005 (2023).
24. Li, X., Xie, S.-P., Gille, S. T. & Yoo, C. Atlantic-induced pan-tropical climate change over the past three decades. *Nat. Clim. Change.* **6**, 275–279 (2016).
25. Lyu, K. & Yu, J. Climate impacts of the Atlantic Multidecadal oscillation simulated in the CMIP5 models: a re-evaluation based on a revised index. *Geophys. Res. Lett.* **44**, 3867–3876 (2017).
26. Cai, W. et al. Pantropical climate interactions. *Science.* **363**, eaav4236 (2019).
27. Johnson, Z. F., Chikamoto, Y., Wang, S.-Y. S., McPhaden, M. J. & Mochizuki, T. Pacific decadal oscillation remotely forced by the equatorial Pacific and the Atlantic Oceans. *Clim. Dyn.* **55**, 789–811 (2020).
28. Meehl, G. A. et al. Atlantic and Pacific tropics connected by mutually interactive decadal-timescale processes. *Nat. Geosci.* **14**, 36–42 (2021).
29. Yao, S., Zhou, W., Jin, F. & Zheng, F. North Atlantic as a trigger for Pacific-Wide decadal climate change. *Geophys. Res. Lett.* **48**, e2021GL094719 (2021).
30. Mo, K. C. & Livezey, R. E. Tropical-extratropical geopotential height teleconnections during the Northern Hemisphere Winter. *Month Weather Rev.* **114**, 2488–2515 (1986).
31. Sardeshmukh, P. D. & Hoskins, B. J. The generation of global rotational flow by steady idealized tropical divergence. *J. Atmos. Sci.* **45**, 1228–1251 (1988).
32. Bjerknes, J. Atlantic Air-Sea Interaction. In *Advances in Geophysics*. (eds. Landsberg, H. E. & Van Mieghem, J.) vol. 10 1–82 (Elsevier, 1964).
33. Visbeck, M. et al. The ocean's response to North Atlantic Oscillation variability. *Geophys. Monogr.-Am. Geophys. Union* **134**, 113–146 (2003).
34. Czaja, A., Robertson, A. W. & Huck, T. The Role of Atlantic Ocean-Atmosphere Coupling in Affecting North Atlantic Oscillation Variability. In *The North Atlantic Oscillation: Climatic Significance and Environmental Impact* 147–172 (American Geophysical Union, 2003).
35. Wang, C. Three-ocean interactions and climate variability: a review and perspective. *Clim. Dyn.* **53**, 5119–5136 (2019).
36. Hamilton, J. D. *Time Series Analysis*. (Princeton University Press, 1994).
37. Granger, C. W. J. Investigating causal relations by econometric models and cross-spectral methods. *Econometrica.* **37**, 424–438 (1969).
38. van Nes, E. H. et al. Causal feedbacks in climate change. *Nat. Clim. Change.* **5**, 445–448 (2015).
39. McGraw, M. C. & Barnes, E. A. Memory matters: a case for Granger causality in climate variability studies. *J. Clim.* **31**, 3289–3300 (2018).
40. Hoskins, B. J. & Karoly, D. J. The steady linear response of a spherical atmosphere to thermal and orographic forcing. *J. Atmosph. Sci.* **38**, 1179–1196 (1981).
41. Wallace, J. M. & Gutzler, D. S. Teleconnections in the geopotential height field during the Northern Hemisphere winter. *Mon. Weather Rev.* **109**, 784–812 (1981).
42. Webster, P. J. Seasonality in the local and remote atmospheric response to sea surface temperature anomalies. *J. Atmos. Sci.* **39**, 41–52 (1982).
43. Branstator, G. Horizontal energy propagation in a barotropic atmosphere with meridional and zonal structure. *J. Atmos. Sci.* **40**, 1689–1708 (1983).
44. Held, I. M. Stationary and quasi-stationary eddies in the extratropical troposphere: Theory. *Large-Scale Dyn. Process. Atmos.* **127**, 168 (1983).
45. Branstator, G. Circumglobal teleconnections, the jet stream waveguide, and the North Atlantic Oscillation. *J. Clim.* **15**, 1893–1910 (2002).
46. O'Brien, J. P. & Deser, C. Quantifying and understanding forced changes to unforced modes of atmospheric circulation variability over the North Pacific in a coupled model large ensemble. *J. Clim.* **36**, 19–37 (2023).
47. Wang, L., Yu, J.-Y. & Paek, H. Enhanced biennial variability in the Pacific due to Atlantic capacitor effect. *Nat. Commun.* **8**, 14887 (2017).
48. Rayner, N. A. et al. Global analyses of sea surface temperature, sea ice, and night marine air temperature since the late nineteenth century. *J. Geophys. Res. Atmos.* **108**, 2670 (2003).
49. Compo, G. P. et al. The twentieth-century reanalysis project. *Q. J. R. Meteorol. Soc.* **137**, 1–28 (2011).
50. Kalnay, E. et al. The NCEP/NCAR 40-year reanalysis project. in *Renewable energy* Vol1_146-Vol1_194 (Routledge, 2018).
51. Kanamitsu, M. et al. Ncep–doe amip-ii reanalysis (r-2). *Bull. Am. Meteorol. Soc.* **83**, 1631–1644 (2002).
52. Hobday, A. J. et al. A hierarchical approach to defining marine heatwaves. *Prog. Oceanogr.* **141**, 227–238 (2016).
53. Scaife, A. A. et al. Tropical rainfall, Rossby waves and regional winter climate predictions. *Q. J. R. Meteorol. Soc.* **143**, 1–11 (2017).
54. Takaya, K. & Nakamura, H. A formulation of a wave-activity flux for stationary Rossby waves on a zonally varying basic flow. *Geophys. Res. Lett.* **24**, 2985–2988 (1997).
55. Plumb, R. A. On the three-dimensional propagation of stationary waves. *J. Atmos. Sci.* **42**, 217–229 (1985).
56. Hurrell, J. W. et al. The community earth system model: a framework for collaborative research. *Bull. Am. Meteorol. Soc.* **94**, 1339–1360 (2013).
57. Hurrell, J. W., Hack, J. J., Shea, D., Caron, J. M. & Rosinski, J. A new sea surface temperature and sea ice boundary dataset for the community atmosphere model. *J. Clim.* **21**, 5145–5153 (2008).
58. Akaike, H. A new look at the statistical model identification. *IEEE Trans. Autom. Control.* **19**, 716–723 (1974).
59. Sugihara, G. et al. Detecting causality in complex ecosystems. *Science.* **338**, 496–500 (2012).

Acknowledgements

This research was funded by the Climate and Large-Scale Dynamics Program of the U.S. National Science Foundation (Grant AGS-2109539). We also gratefully acknowledge NASA Award NNH19ZHA001C to the California Space Grant Consortium (CalSpace) for additional support. High-performance computing resources were provided by the National Center for Atmospheric Research (NCAR) Computational and Information Systems Laboratory, sponsored by the National Science Foundation. We thank the two anonymous reviewers for their constructive feedback that helped improve the manuscript.

Author contributions

J.-Y.Y. and Y.Z. conceptualized and designed the study. Y.Z. conducted the data analysis and created the figures. The initial draft of the manuscript was written by Y.Z. and J.-Y.Y. All authors, including Y.Z. and J.-Y.Y., participated in interpreting the results and contributed to subsequent revisions of the manuscript.

Competing interests
The authors declare no competing interests.

Additional information
Supplementary information The online version contains supplementary material available at https://doi.org/10.1038/s41612-025-01187-6.

Correspondence and requests for materials should be addressed to Jin-Yi Yu.

[1]Department of Earth System Science, University of California, Irvine, CA, USA. [2]Research Center for Environmental Changes, Academia Sinica, Taipei, Taiwan. [3]Department of Atmospheric Sciences, National Taiwan University, Taipei, Taiwan. [4]School of Atmospheric Sciences, Sun Yat-sen University, and Southern Marine Science and Engineering Guangdong Laboratory (Zhuhai), Zhuhai, China. [5]Guangdong Province Key Laboratory for Climate Change and Natural Disaster Studies, Sun Yat-sen University, Zhuhai, China. [6]State Key Laboratory of Tropical Oceanography, South China Sea Institute of Oceanology, Chinese Academy of Sciences, Guangzhou, China. [7]Global Ocean and Climate Research Center, South China Sea Institute of Oceanology, Chinese Academy of Sciences, Guangzhou, China. [8]Guangdong Key Laboratory of Ocean Remote Sensing, South China Sea Institute of Oceanology, Chinese Academy of Sciences, Guangzhou, China. [9]Frontier Science Center for Deep Ocean Multispheres and Earth System (FDOMES) and Physical Oceanography Laboratory, Ocean University of China, Qingdao, China. [10]College of Oceanic and Atmospheric Sciences, Ocean University of China, Qingdao, China. [11]Guangdong Key Laboratory of Ocean Remote Sensing, State Key Laboratory of Tropical Oceanography, South China Sea Institute of Oceanology, Chinese Academy of Sciences, Guangzhou, China. [12]State Key Laboratory of Satellite Ocean Environment Dynamics, Second Institute of Oceanography, Ministry of Natural Resources, Hangzhou, China. [13]Department of Marine Science and Convergence Engineering, Hanyang University, ERICA, Ansan, Republic of Korea. ✉e-mail: jyyu@uci.edu

Geophysical Research Letters

Supporting Information for

A shifting tripolar pattern of Antarctic sea ice concentration anomalies during multi-year La Niña events

Tingting Zhu[1] and Jin-Yi Yu[1]

[1]Department of Earth System Science, University of California, Irvine, CA, USA

Contents of this file

Texts S1

Figures S1-S5

Text S1. Definitions of climate indices used in this study

Three indices based on sea surface temperature anomalies (SSTAs) in the tropics were used in the study. The IOD index (Saji et al. 1999) is defined as the SSTA difference between western Indian Ocean (50°-70°E, 10°S-10°N) and eastern Indian Ocean (90°E-110°E, 10°S-0°S). Following Kim and Yu (2022), a zonal location (ZL) index of El Niño-Southern Oscillation (ENSO) is defined as the difference between the SSTAs averaged over the tropical eastern Pacific (100°-160°W, 5°S-5°N) and the SSTAs averaged over the tropical central Pacific (150°E-160°W, 5°S-5°N). Positive ZL values indicate that the La Niña events are located more within the tropical central Pacific (CP) and are of the so-called CP type of ENSO (Yu and Kao 2007; Kao and Yu 2009), while negative values indicate the events are located more within the tropical eastern Pacific (EP) and are of the so-called EP type of ENSO. The tropical north Atlantic (TNA) index is defined as the SSTAs averaged between 15°-55°W and 5°-25°N.

Figure S1. Composite SSTAs (°C) for the single-year La Niñas occurring during years 400 to 2200 of the CESM1 Pre-industrial simulation: (a) longitude–time plot of equatorial (5°S–5°N) Pacific SSTAs (shaded; °C) from June^{-1} to December^{+2}; (b) composite SSTA pattern during JJA^{0}; and (c) values of the composite IOD, ZL and TNA indexes during JJA^{0}. Dots indicate areas where the values exceed the 95% confidence interval determined using a two-tailed Student's t test.

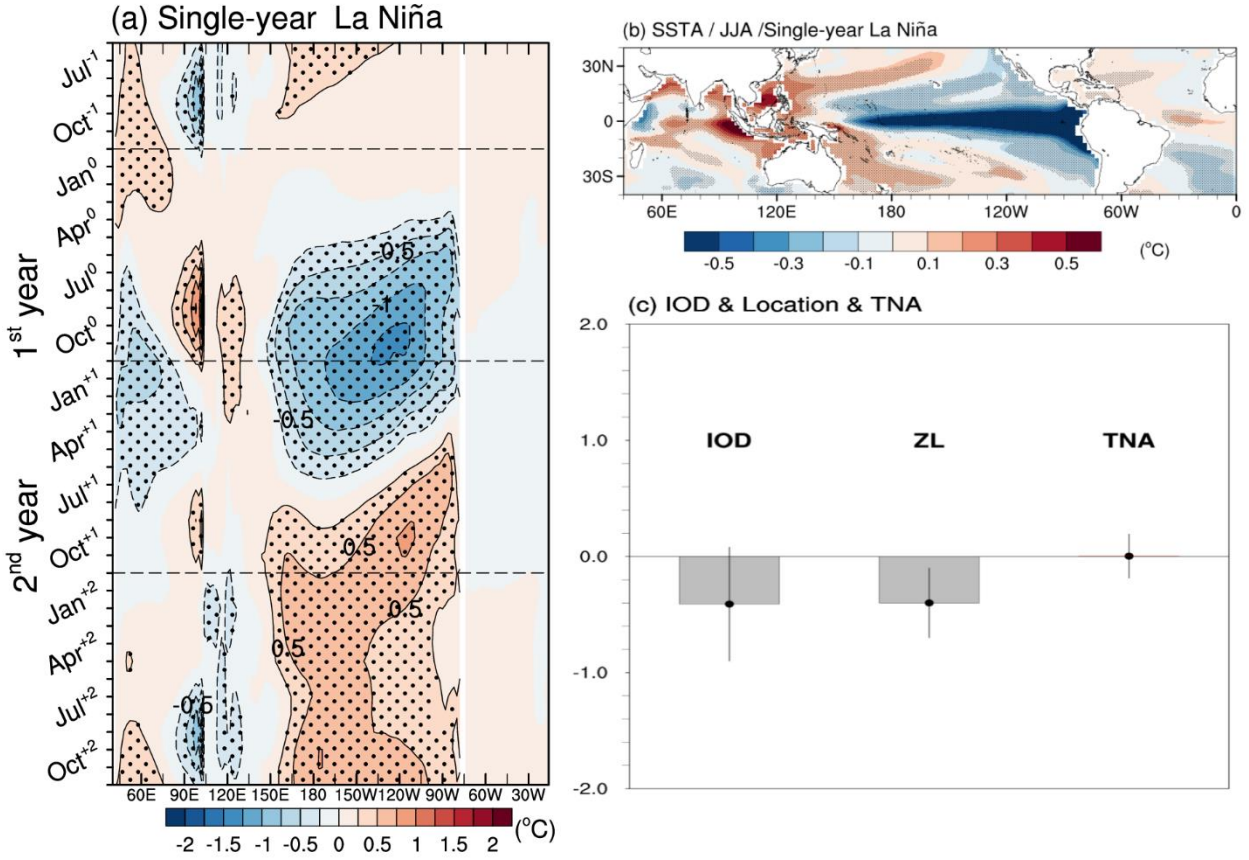

Figure S2. Composite anomalies in sea ice concentration (SIC; top panels), surface air temperature (SAT; °C, middle panels), and sea level pressure (SLP; hPa, bottom panels) for the simulated (left two columns of panels) and observed (right two columns of panels) multi-year La Niñas during the first austral winter (JJA^{0}; first and third-column panels) and second austral winter (JJA^{+1}; second and fourth-column panels). The simulated events are selected from years 400-2,200 of the CESM1 Pre-industrial simulation and the observed events are selected from the period 1979-2020. The outermost latitude circles in the top and middle panels are the 55° latitude, while it is the 30° latitude in the bottom panels. Composite surface wind vectors are superimposed in the middle and bottom panels. Dots indicate areas where the values exceed the 95% confidence interval determined using a two-tailed Student's t test.

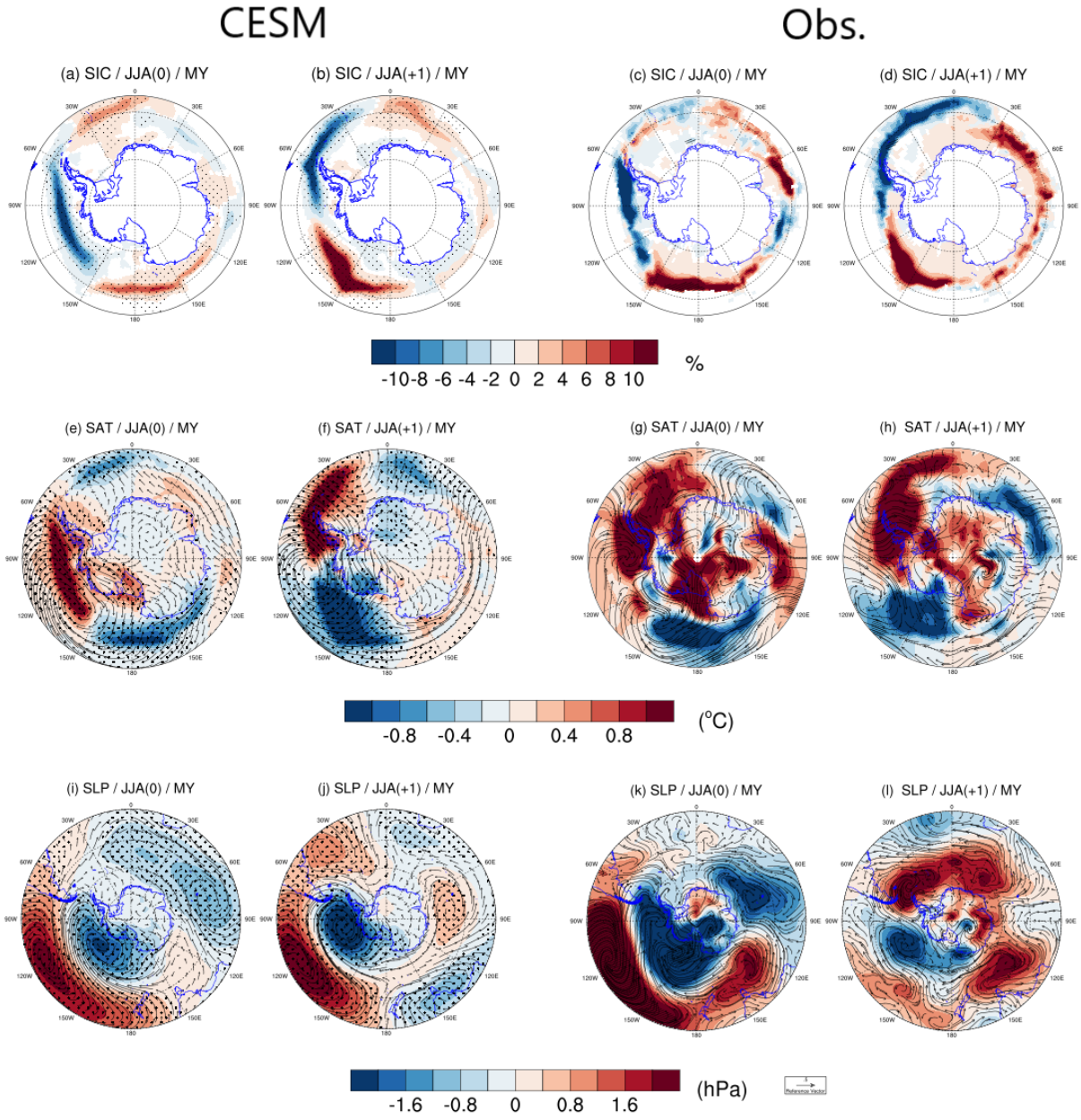

Figure S3. Composite characteristics of multi-year La Niñas observed during the period 1979-2020: (a) longitude–time plot of equatorial (5°S–5°N) Pacific SSTAs (shaded; °C) from June^{-1} to December^{+2}; (b) composite SSTA pattern during the first austral winter (JJA^{0}) of the vent; (c) composite SSTA pattern during the second austral winter (JJA^{+1}); and (d) values of the composite IOD, ZL and TNA indexes during the JJA^{0} (red bar) and JJA^{+1} (blue bar). Dots indicate areas where the values exceed the 95% confidence interval determined using a two-tailed Student's t test.

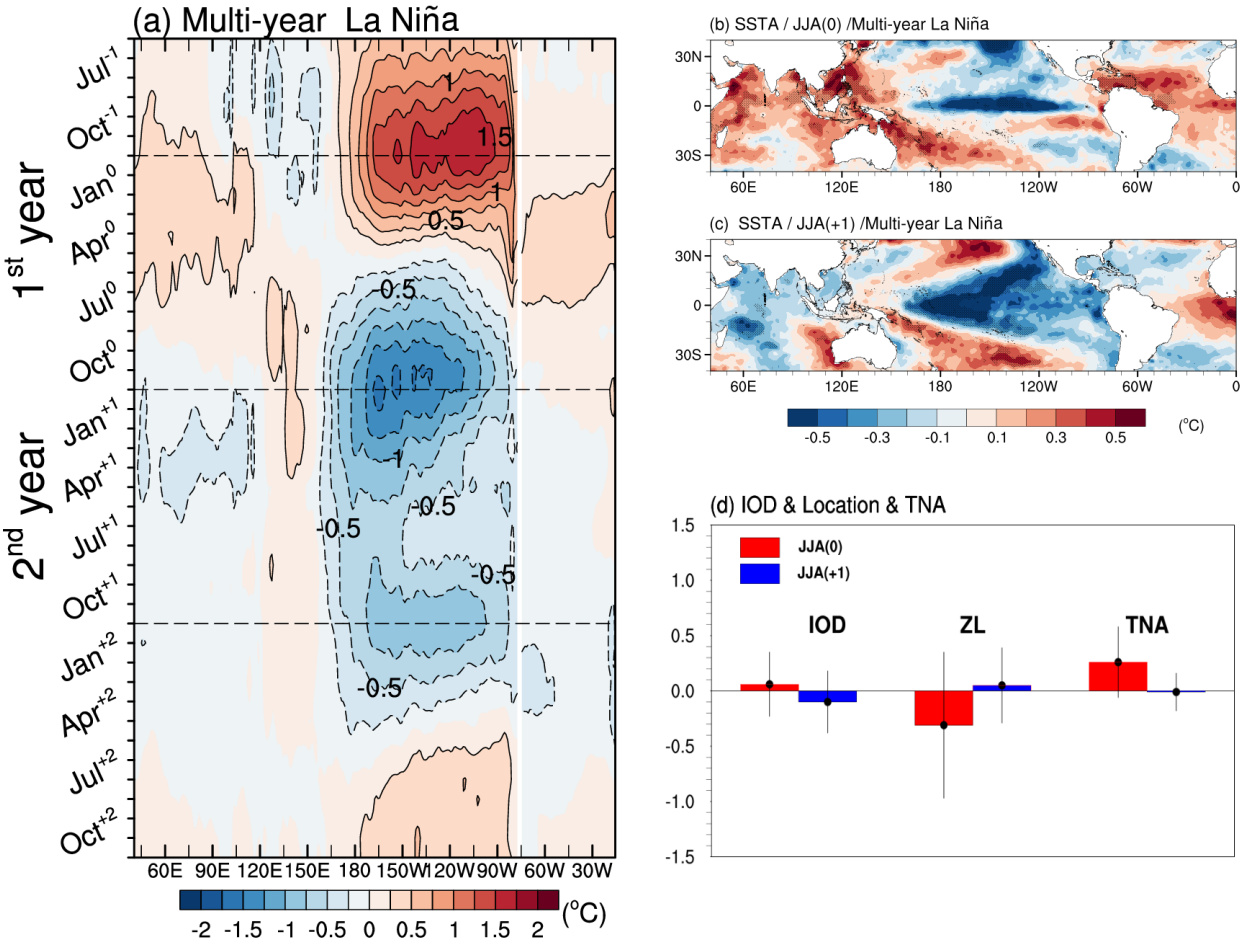

Figure S4. Same as Figure S3 but for the composite of observed single-year La Niña events.

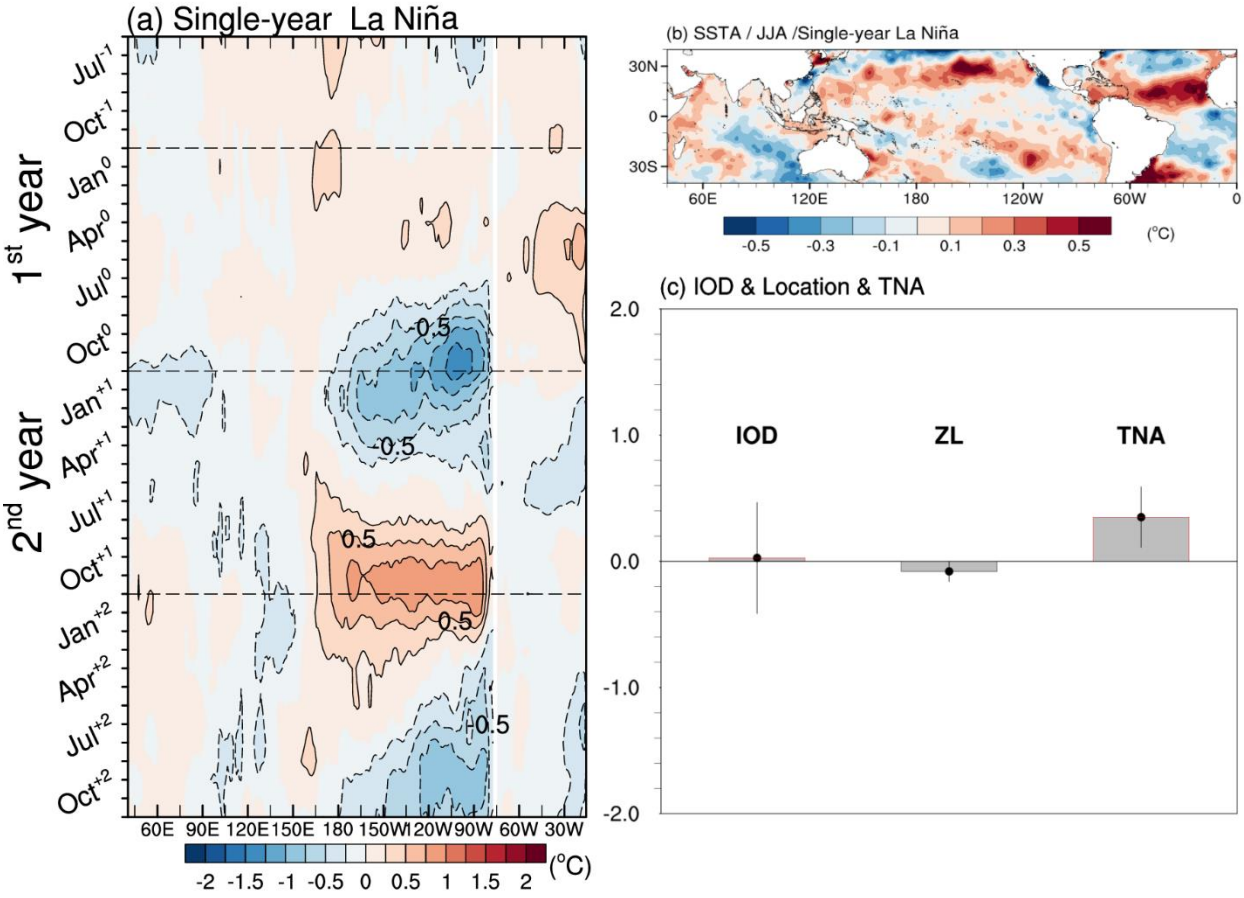

Figure S5. (a) The SIC anomalies during the first (JJA^{0}) and second (JJA^{+1}) austral winters of the six multi-year La Niña events observed during the period 1979-2020.

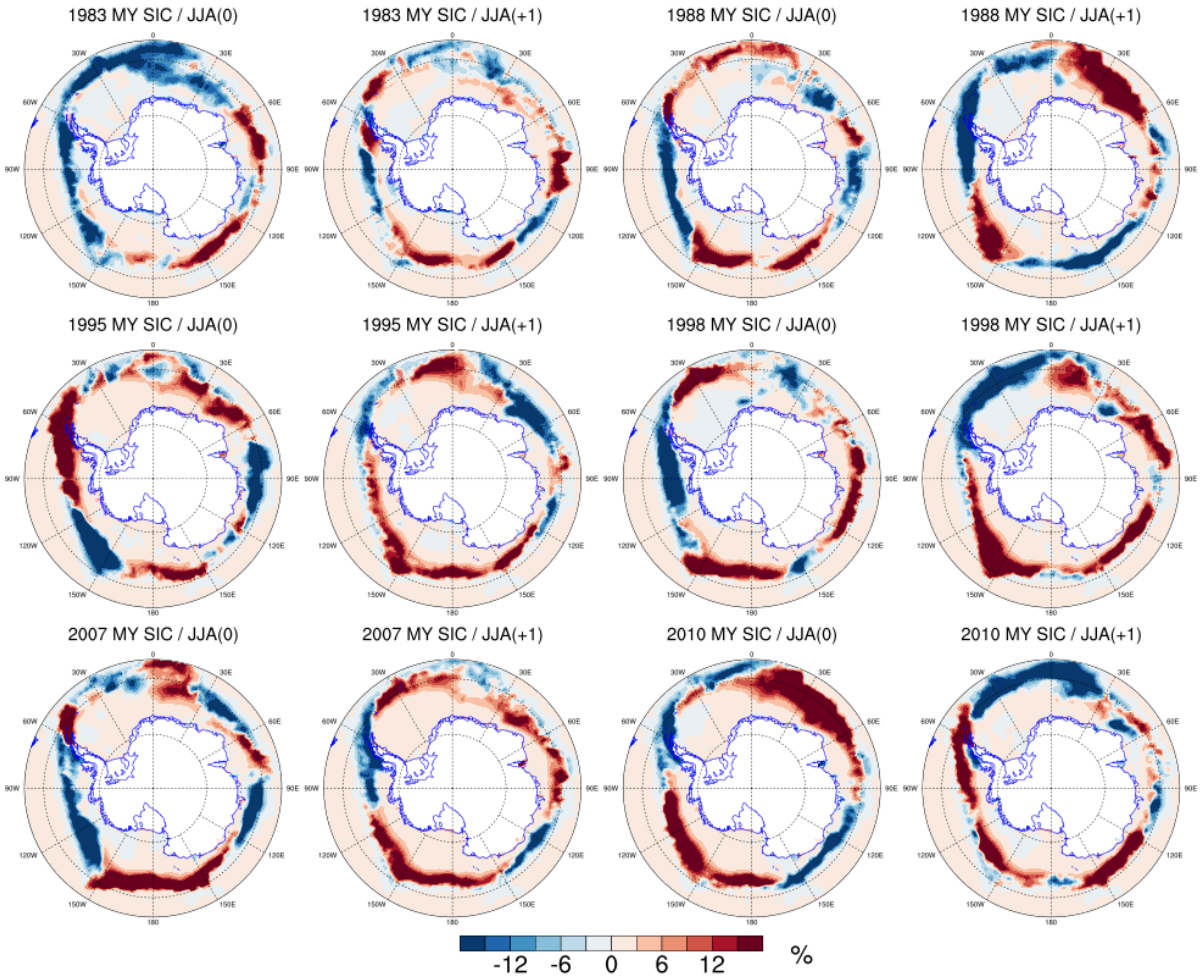

Reference

Kao, H. Y., & Yu, J. Y. (2009). Contrasting eastern-Pacific and central-Pacific types of ENSO. Journal of Climate, 22(3), 615-632.

Kim, J.-W. & Yu, J.-Y. (2022): Single- and multi-year ENSO events controlled by pantropical climate interactions, npj Climate and Atmospheric Science, DOI:10.1038/s41612-022-00305-y.

Saji, N. H., Goswami, B. N., Vinayachandran, P. N., & Yamagata, T. (1999). A dipole mode in the tropical Indian Ocean. Nature, 401(6751), 360.

Yu, J.-Y. & Kao, H.-Y. (2007). Decadal Changes of ENSO Persistence Barrier in SST and Ocean Heat Content Indices: 1958-2001. Journal of Geophysical Research, 112, D13106, doi: 10.1029/2006JD007654.